Desalination and Water Treatment
www.deswater.com

doi: 10.5004/dwt.2017.21481

92 (2017) 145–151
October

Preparation of mesoporous TiO_2–SiO_2 by ultrasonic impregnation method and effect of its calcination temperature on photocatalytic activity

Azadeh Haghighatzadeh[a,*], Babak Mazinani[b], Mohammadreza Shokouhimehr[c], Leila Samiee[d]

[a]*Physics Group, Department of Sciences, Ahvaz Branch, Islamic Azad University, P.O. Box 61349-68875, Ahvaz, Iran, email: azadeh.haghighatzadeh.physics@gmail.com*
[b]*Department of Materials Engineering, Malayer University, Malayer, Iran, email: b.mazinani@gmail.com*
[c]*School of Metallurgy and Materials Engineering, Iran University of Science and Technology, Tehran 16846, Iran*
[d]*Research Institute of Petroleum Industry (RIPI), West Entrance Blvd., Olympic Village, P.O. Box: 14857-33111, Tehran, Iran*

Received 1 April 2017; Accepted 20 September 2017

ABSTRACT

This article presents a novel procedure to synthesis mesoporous TiO_2–SiO_2 structure via ultrasonic impregnation method. Mesoporous silica SBA-15 as a host structure was first prepared. Then, the prepared host structure was mixed with a homogenized solution of TiO_2 precursor under ultrasonic condition at 40°C. To understand the chemical composition and structural properties of the synthesized powder, several characterization techniques such as powder X-ray diffraction, small-angle X-ray scattering, nitrogen adsorption, X-ray photoelectron spectroscopy, transmission electron microscopy, field-emission scanning electron microscopy and energy dispersive X-ray were employed. Photocatalytic activity of the calcined materials at various temperatures (400°C, 600°C, and 800°C) was evaluated by degradation of methylene blue solution under UV light. The anatase crystals were the only detected phase until 800°C due to formation of Ti–O–Si bonds. Photo-degradation results revealed that all of synthesized samples possess much more photocatalytic activity than commercial TiO_2. In addition, a higher photocatalytic efficiency was achieved at higher calcination temperature owing to more degree of crystallinity.

Keywords: Mesoporous; Photocatalyst; TiO_2; SiO_2

1. Introduction

Titanium oxide has been known as one of the most important photocatalysts for both academic research and industrial applications, especially water treatment and degradation of organic compounds, because of its great photocatalytic efficiency, chemical stability, low price and non-toxicity [1–4]. The photocatalytic efficiency of TiO_2 particles depends on crystal phase, size, shape, surface area and structure [5]. There are three different common crystal structure of TiO_2 known as rutile, anatase, and brookite. Each crystal structure shows certain physical, chemical, and optical properties that may affect their properties and catalytic efficiency. The anatase phase of TiO_2 generally presents the highest photocatalytic activity. However, the rutile crystal structure is the most stable phase thermodynamically and has low band gap energy which increases the corresponding photoabsorption in the visible region [6,7].

The application of commercial TiO_2, for example, P-25 (Degussa, Germany) in water cleaning systems where wastewater is contaminated with pollutants has been intensively investigated [8–11]. The catalytic activity is related to active sites and accessible surface of TiO_2, but the most commercial products have generally small particle size which hinders their recovery and reuse after the completion of the processes. In addition, the difficulty arising in catalyst-recovering limits their practical application. These ultra-fine powders generally

* Corresponding author.

tend to agglomerate into large size particles, resulting in loss of catalytic activity [12]. To address these issues, synthesis of mesoporous TiO_2 nanostructures has been recently explored as a solution. Mesoporous TiO_2 not only represents a high surface area, but also has larger particle sizes which can be filtered much easier compared with TiO_2 nanoparticles [13,14]. However, there are still several problems to achieve ideal mesoporous TiO_2 with high crystallization, large surface area and anatase phase properties [15–17]. For example, one of the challenges in the synthesis of mesoporous TiO_2 is quick hydrolysis and condensation of Ti precursors [18,19]. To resolve the aforementioned problems, researchers have recently focused on incorporating TiO_2 within a mesoporous SiO_2 matrix due to two important reasons: (1) formation of Ti–O–Si bonds can retain anatase phase at high calcination temperatures [4,20,21] and (2) introducing titanium species into mesoporous silicate materials provides much higher active surface areas compared with purely made mesoporous titania [22]. Furthermore, the necessities to develop appropriate synthetic methods have persuaded researchers to explore feasible procedures for obviating the existing drawbacks and obtaining homogeneous mesoporous TiO_2–SiO_2 frameworks.

In the present paper, we report a novel route to incorporate TiO_2 into mesoporous silica host structure through ultrasonic method at 40°C. Ultrasound increases the penetration of sol into the pores and continuing this treatment improves the effect with rising temperature [23]. Further, the effect of calcination temperature and crystal phases on photocatalytic activity was evaluated.

2. Experimental

2.1. Materials

Pluronic triblock copolymer P123 poly (ethylene glycol)–poly (propylene glycol)–poly (ethylene glycol), Mw = 5,800 and titanium isopropoxide (TTIP) were purchased from Aldrich (Germany). Tetraethoxysilane (TEOS), anhydrous ethanol and HCl (37% concentration) were obtained from Merck (Germany). Methylene blue (>97%) was purchased from Sigma-Aldrich and p25 titanium dioxide was bought from Evonik (Germany).

2.2. Preparation of mesoporous TiO_2–SiO_2 composites

The method selected for preparation of host structure mesoporous SiO_2 involves the following procedure: 4 g of P123 was dissolved in 30 g water and 120 g HCl (2 M) solution and stirred for 5 h at 40°C in a closed bottle. TEOS (9 g) was added to the stirring solution. The mixture was stirred for 24 h in a closed bottle and then transferred to a Teflon-lined autoclave for further aging at 100°C for 48 h. All materials were filtered, washed with deionized water, and dried. The solid product was calcined at 540°C to remove the remaining surfactant. The prepared mesoporous silica structure designated as SW.

For mesoporous TiO_2–SiO_2 synthesis, TTIP (3.55 g) was mixed with pure ethanol (9.72 g). The mixture was capped and placed in an ultrasonic bath at 40°C. Then mesoporous silica host structure was added (weight ratio of SiO_2/TiO_2 = 2) and the mixture was treated for 4 h under ultrasonic irradiation at 40°C. Then, the solvent was evaporated at room temperature. Finally, the obtained powder was heat treated at different calcination temperatures (400°C, 600°C, 800°C and 1,000°C). The prepared materials are designated as SW-*x*, where *x* is calcination temperature.

2.3. Characterization

Water was deionized by using a Nanopure System (Barnsted). Small-angle X-ray scattering (SAXS) patterns were collected on a Kratky compact small-angle system using Kα radiation at 40 kV and 20 mA, equipped with a position-sensitive detector containing 1,024 channels of width 53.0 mm. Surface areas were evaluated by using nitrogen absorption–desorption (Brunauer–Emmett–Teller [BET])-autosorb-1 from Quantachrome Instruments after degassing of samples at 250°C for 6 h. Powder X-ray diffraction (XRD) patterns were recorded with a Bruker powder X-ray diffractometer using a Cu radiation source of wavelength 1.54 Å with a scan speed of 0.04° per second at 40 kV and 40 mA. The morphology of the samples was characterized by a scanning electron microscope (SEM, LEO-1525) with an accelerating voltage of 20 kV. X-ray photoelectron spectroscopy (XPS) spectra were recorded with Omicron Nanotechnology (ELS5000) system using Al Kα radiation at a base pressure below 5.5×10^{-9} Torr. Transmission electron microscopy (TEM) was performed with a Philips Tecnai 20 microscope operated at 200 kV. The chemical bonds were analyzed by Fourier-transform infrared spectrophotometry (FTIR; Perkin–Elmer) from 4,000–400 cm^{-1}.

2.4. Photocatalytic activity measurement

The photocatalytic activity of the prepared samples was evaluated by degradation of methylene blue in aqueous solution under UV light irradiation (mercury lamp 125 W). In total, 30 mg of commercial Evonik P25 was dispersed in 100 mL MB solution having a concentration 40 mg/L. Quantities of mesoporous TiO_2/SiO_2 used as photocatalysts were calculated to achieve an identical TiO_2 loading in the systems. The mixture was first reacted for 30 min under dark condition. The concentration spectra of the mixtures were recognized using UV–Vis spectrometry after centrifugation.

3. Results and discussion

SAXS patterns of samples before and after impregnation are presented in Fig. 1. SW sample clearly shows three Bragg peaks, which is characteristic of (100), (110) and (200) diffraction planes of the hexagonal pore structure [24]. The hexagonal unit cell of SW and SW-600 samples are 13.08 and 12.36 nm, respectively (according to the equation: $a_0 = 2d_{100}/\sqrt{3}$). However, the peak intensity and peak position of SW-600 were changed compared with SW.

The weaker diffraction peaks indicate poorer pore structure organization of SW-600, while the peak shifts suggesting that pore to pore distances have decreased in SW-600 due to a higher calcination temperature and consequently more condensation of silica walls compared with SW. The calculated wall thickness of samples is presented in Table 1. Although at higher calcination temperature, the wall thickness is expected to be formed as thin layers due to

higher condensation level, SW-600 has higher wall thickness in value compared with SW confirms the formation of TiO_2 particles and layers inside the channels of host structure.

As seen in Fig. 2, the N_2 adsorption–desorption isotherms of SW exhibits isotherm type IV with H1 hysteresis loops according to IUPAC category [25]. The isotherm is characteristic of mesoporous materials with two dimensional hexagonal arrangement of channels [26]. The SW sample presents the hysteresis loop at relative pressures (P/P_0) in the range of 0.6–0.8 that represents the spontaneous filling of the mesopores owing to capillary condensation, representing the presence of uniform mesopores.

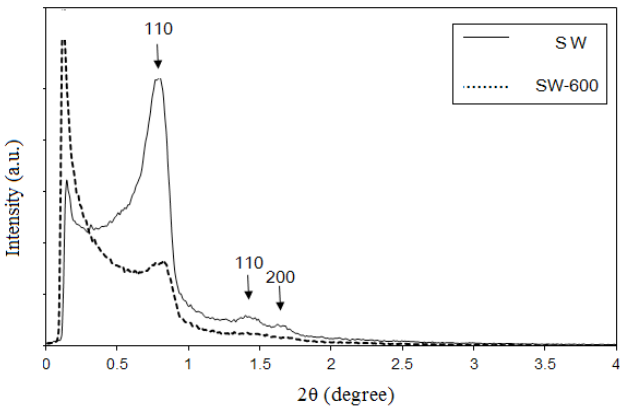

Fig. 1. SAXS patterns of SW and SW-600.

Table 1
Textural properties of SW and SW-600 mesoporous materials

Sample	SW	SW-600
S_{BET} (m^2/g)[a]	665.7	395.2
V_{total} (cm^3/g)[b]	1.023	0.672
D_p (nm)[c]	9.59	7.93
d_{100} (nm)	11.32	10.7
a (nm)[d]	13.08	12.36
t (nm)[e]	3.49	4.43

[a]BET surface area.
[b]Adsorption total pore volume.
[c]BJH pore diameter calculated from adsorption branch of the isotherm.
[d] $a = 2d_{100}/\sqrt{3}$.
[e]Pore wall thickness is equal to $a - D_p$.

It can be clearly seen that the presence of TiO_2 into SW leads to a significant difference in shape of hysteresis loops between SW and SW-600 samples. SW-600 shows isotherm type IV with H2(b) hysteresis loop indicating the existence of pore necks due to impregnation of TiO_2 particles inside the channels [27]. The Barrett–Joyner–Halenda (BJH) pore size distributions of samples according to adsorption branch are presented in Fig. 2(b). A reduction of pore sizes after impregnation of TiO_2 is clear. The structural characteristics of the SW and SW-600 samples are summarized in Table 1. Based on these results, due to TiO_2 impregnation, the surface area decreased from 665.7 to 395.1 m^2/g. In addition, the total pore volume reduced from 1.023 to 0.672 cm^3/g as derived from the amount of N_2 adsorbed at p/p_0 of 0.99.

Fig. 3(a) shows the O1s core level spectra of SW-600 sample. The spectrum of this sample can be fitted by three Lorentzian curves due to its asymmetry appearing at 533.2 (peak 3), 532 (peak 2) and 530.6 eV (peak 1), which can be ascribed to the binding energy of Si–O–Si, Si–O–Ti and Ti–O–Ti components, respectively [28–30]. The appearance of peak on 532 eV indicates that TiO_2 and SiO_2 are attached by chemical bonds. The oxygen in the SiO_2 and TiO_2 are at the tetrahedral and octahedral site, respectively [31].

The formation of Ti–O–Si bonds is approved by FTIR result as well (Fig. 3(b)). The Ti–O–Si infrared vibration is generally detected between 910 and 960 cm^{-1} [32,33], with the exact band position depending on the chemical composition of the sample as well as calibration and resolution of the instrument [34]. The presence of a strong band at 960 cm^{-1} in the sample suggests that the formation of a large amount of Ti–O–Si linkages. The bands at 1,100 and 800 cm^{-1} are assigned to the asymmetric and symmetric stretching vibrations in Si–O–Si framework, respectively [31]. Moreover, the spectral peaks around 3,400 and 1,650 cm^{-1} are attributed to the stretching mode of water hydroxyl bonds [35].

TEM image of SW-400 confirms the formation of well-ordered channels with an average diameter of 6–10 nm (Fig. 4(a)). The uniform pore size is in good agreement with the value of N_2 adsorption–desorption results. EDX analysis of the selected region A also shows a high concentration of Ti (Fig. 4(a) inset). Fig. 4(b) shows SEM micrograph of SW-400.

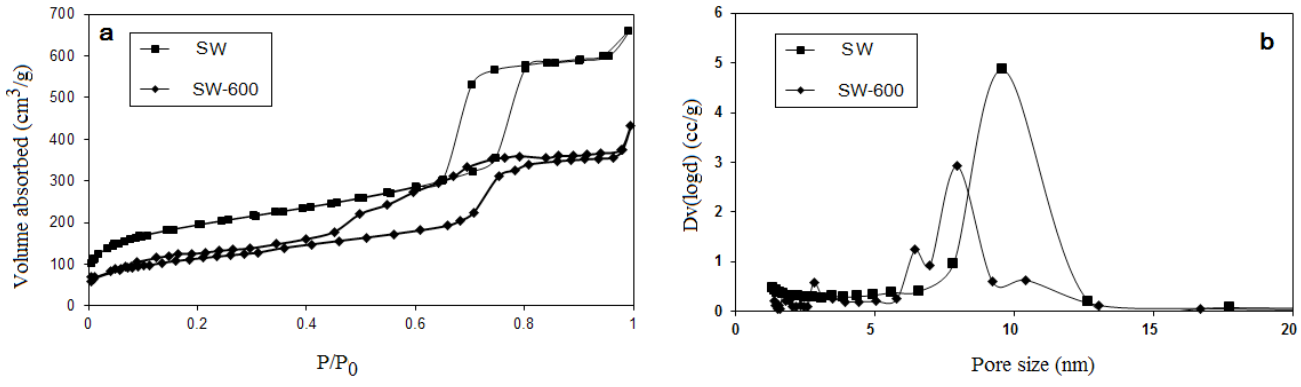

Fig. 2. N_2 adsorption–desorption isotherms (a) and the corresponding pore size distributions (b) for SW and SW-600.

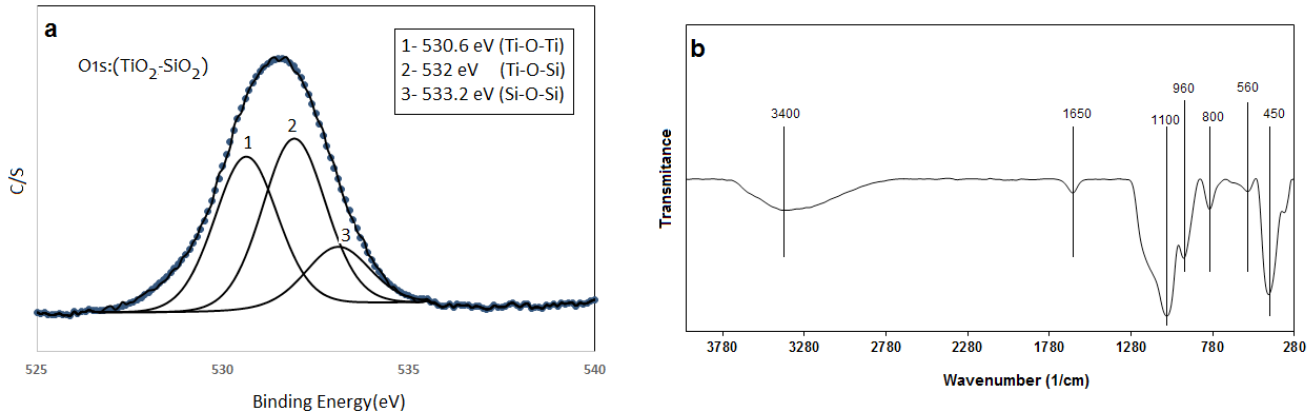

Fig. 3. XPS (a) and FTIR (b) patterns of SW-600 sample.

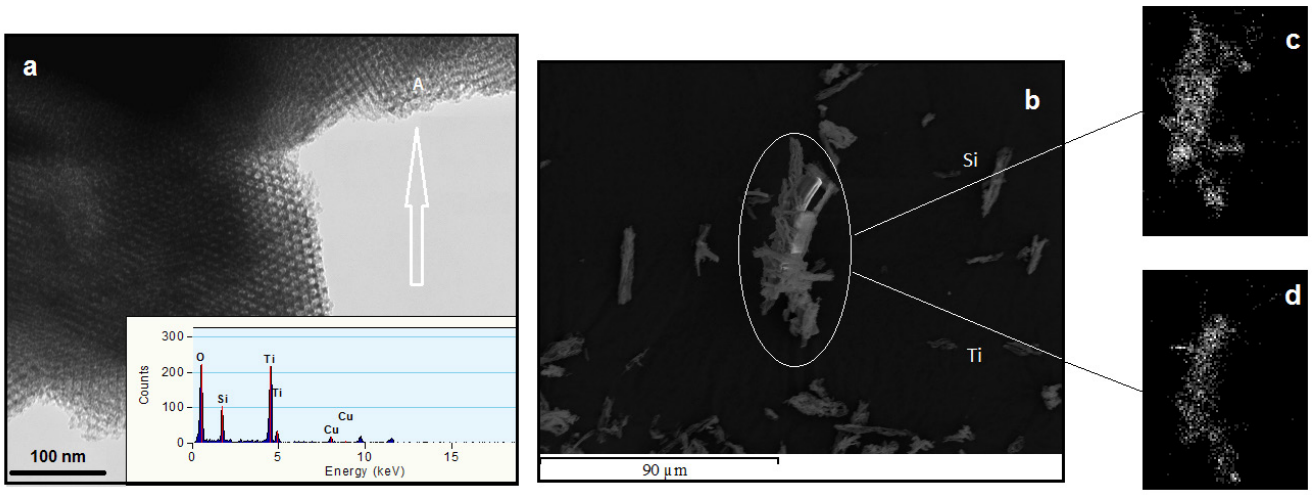

Fig. 4. (a) TEM micrograph of SW-400. The inset exhibits EDX analysis of Point A. (b) SEM images of SW-400 and (c and d) the related EDX maps for Si and Ti of the selected area.

According to the previously published papers, the shape of silica particles would be rod like before impregnation using this synthesis procedure [36]. It can be seen that rod like shape of particles have been retained after impregnation and there is no separate agglomerated TiO_2 crystals. As it is shown in X-ray energy dispersive maps of Fig. 4(b), TiO_2 and SiO_2 are homogeneously distributed in the structure. It should be mentioned the weight ratio of this sample was adjusted as $SiO_2/TiO_2 = 2$, therefore, Si can be detected more by EDX analysis.

The powder XRD patterns of samples are shown in Fig. 5. As it can be seen until 800°C, anatase is the only detected phase of the samples. The phase transformation from anatase to rutile can be recognized at 1,000°C. The average size of crystallites was calculated using the Scherrer equation [37]:

$$d = \frac{0.9\lambda}{\beta\cos\theta} \quad (1)$$

where 0.9 is a shape factor of the particle, λ and θ are the wavelength and the incident angle of the X-rays, respectively.

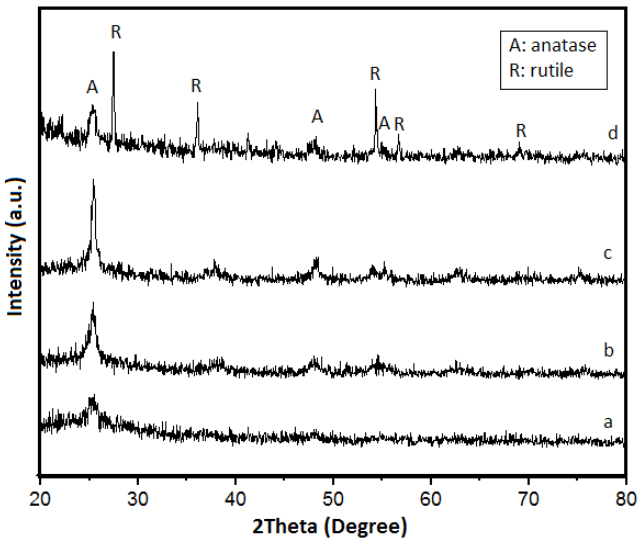

Fig. 5. WAXRD patterns of (a) SW-400 (b) SW-600 (c) SW-800 and (d) SW-1000.

β is the half width of the peak at the 2θ value. As the temperature raised from 400°C to 800°C, the peaks of anatase crystal become stronger and shaper, and the grain size was determined from the width at half maximum of the anatase (101) peak (Table 2). The transformation of anatase to rutile phase happened at 1,000°C. Anatase can be transformed irreversibly to rutile in pure TiO_2 at calcination temperature around 400°C [38]. It is proved that the existence of silica inhibits the transformation of anatase to rutile phase and the growth of crystal grain at elevated temperatures which can be related to existence of Ti–O–Si bonds [21]. It has been reported that a critical size must be reached for the phase transition from the anatase to rutile in titania particles [39].

Therefore, this high thermal stability makes TiO_2–SiO_2 components susceptible for calcination at higher temperature without formation of rutile phase, and to form anatase crystals with high crystallinity. It has been shown that the photodegradation efficiency is much more rapid over anatase than rutile [40,41].

Table 2
Crystal size and photocatalytic efficiency of samples

Sample	Crystal size Anatase/Rutile (nm)[a]	Photocatalytic efficiency (%)[b]
SW-400	3.2/–	26.2
SW-600	5.4/–	17
SW-800	8.2/–	30.1
SW-1000	5.1/27.2	–

[a]Calculated according to Eq. (1).
[b]Photocatalytic efficiency according to Eq. (2).

In order to investigate the effect of calcination temperature on photocatalytic activity of samples, MB degradation under UV light was carried out (Fig. 6). The process of photodegradation starts when TiO_2 photocatalyst absorbs a UV radiation of energy equal or higher than its band gap (3.2 eV for anatase and 3.0 eV for rutile). Then, the electron and the hole are generated in the conduction band and in the valence band of TiO_2, respectively. Hydroxide ions or water molecules can be oxidized by the positive holes to generate hydroxyl radical. On the other hand, superoxide radical anions can be produced by reaction of oxygen molecules and the electrons of conduction band. Most azo dyes such as methylene blue can be oxidized by resulting hydroxyl radicals [42,43]. As it can be seen in Figs. 6(a)–(c), the maximal absorbance declined as the exposure time increased and was measured to characterize the degradations efficiency of the samples. Before the UV light irradiation, the mixtures containing the catalysts and MB were stirred in the dark for 30 min to ensure that the adsorption–desorption equilibrium of MB was established. Fig. 6(d) shows the photocatalytic performance of samples calcined at different temperature (400°C, 600°C, and 800°C) comparing with that of a commercial anatase TiO_2 (P 25, Degussa), which is the standard system employed in the field of photocatalytic reactions. P25 was evaluated under similar

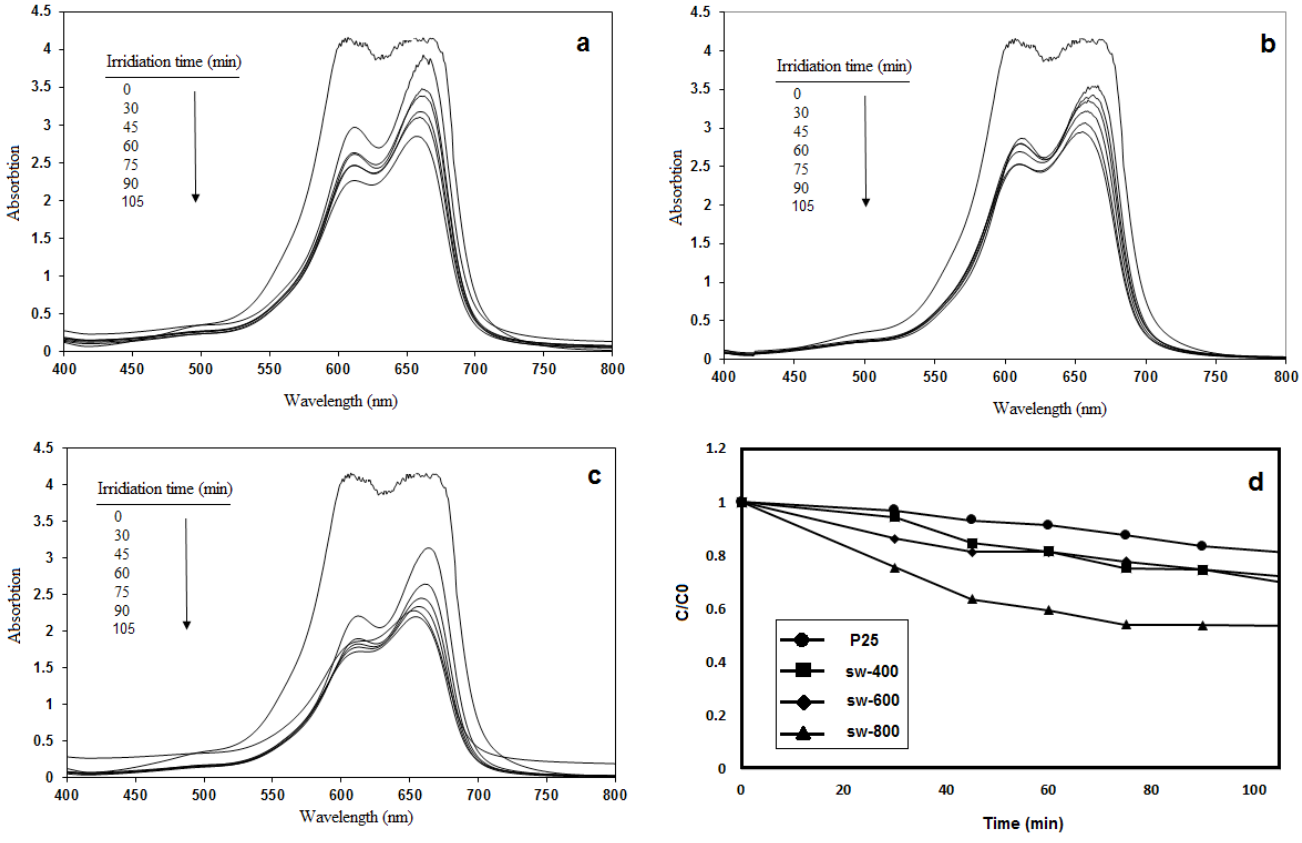

Fig. 6. UV–Vis absorption spectra of MB dye by (a) SW-400, (b) SW-600 and (c) SW-800. (d) Degradation curves of MB by the samples.

condition in order to compare results. This reference material contains anatase and rutile phases in a ratio of about 3:1 and it has a specific area of 49.2 m^2/g [44]. The photocatalytic decomposition rate of samples was determined using the following equation:

$$\text{Photocatalytic decomposition rate} = \frac{C_0 - C}{C_0} \quad (2)$$

where C_0 is the initial concentration of the MB solution before dark condition and C is the final concentration after illumination. Hence, decolonization efficiency can be calculated according to Eq. (3) and the results are presented in Table 2.

$$\text{Efficiency} = \frac{C_0 - C}{C_0} \times 100 \quad (3)$$

Photocatalytic efficiency of mesoporous SiO_2–TiO_2 can be improved by an increase of surface area of composite and degree of crystallinity of TiO_2 crystals. Although higher calcination temperatures increases degree of crystallinity, it decreases the surface area [4,20,21,36]. According to Table 1, all samples have a higher photoactivity compared with P25. SW-800 shows the highest photocatalytic efficiency (30.1%) which can be attributed to high degree of crystallinity. SW-400 shows a higher photoactivity than SW-600 which can be related to greater surface area of SW-400 compared with SW-600. Higher calcination temperature (1,000°C) led to a dramatic decline of photocatalytic efficiency (not shown here) which can be attributed to phase transformation of anatase to rutile, grain growth and pore plugging [21].

4. Conclusions

TiO_2 sol was impregnated into mesoporous silica matrix by using ultrasonic radiation at 40°C. A combination of XRD, SAXS, FTIR, XPS, nitrogen adsorption–desorption isotherm measurement, TEM, SEM as well as UV–Vis spectroscopy has been used to characterize the prepared materials. Achieved results demonstrated that TiO_2 particles have been formed inside the channels of host structure and distributed homogeneously. In addition, formation of Ti–O–Si bonds retain phase transformation from anatase to rutile until 800°C which led to achieving high degree of crystallinity of anatase particles, and consequently high photocatalytic efficiency of prepared materials.

Acknowledgments

The work is supported by the Ahvaz Branch of Islamic Azad University. The authors would like to thank the Research Council for their generous support of this work. We are also grateful for their assistance of SIRIM Bhd.

References

[1] J.-W. Shi, H.-J. Cui, X. Zong, S. Chen, J. Chen, B. Xu, W. Yang, L. Wang, M.-L. Fu, Facile one-pot synthesis of Eu, N-codoped mesoporous titania microspheres with yolk-shell structure and high visible-light induced photocatalytic performance, Appl. Catal. A, 435 (2012) 86–92.

[2] Y. Wang, M. Zhong, F. Chen, J. Yang, Visible light photocatalytic activity of TiO_2/D-PVA for MO degradation, Appl. Catal. B, 90 (2009) 249–254.

[3] S.M. Ibrahim, A.K. Masrom, B. Mazinani, S. Radiman, F.M. Jamil, A. Beitollahi, N. Negishi, N. Yahya, Mesoporous titania photocatalyst: effect of relative humidity and aging on the preparation of mesoporous titania and on its photocatalytic activity performance, Res. Chem. Intermed., 39 (2013) 1003–1014.

[4] B. Mazinani, A. Beitollahi, S. Radiman, A.K. Masrom, S.M. Ibrahim, J. Javadpour, F.M.D. Jamil, The effects of hydrothermal temperature on structural and photocatalytic properties of ordered large pore size TiO_2–SiO_2 mesostructured composite, J. Alloys Compd., 519 (2012) 72–76.

[5] H.B. Yener, erife Helvac, Effect of synthesis temperature on the structural properties and photocatalytic activity of TiO_2/SiO_2 composites synthesized using rice husk ash as a SiO_2 source, Sep. Purif. Technol., 140 (2015) 84–93.

[6] T. Kawahara, Y. Konishi, H. Tada, N. Tohge, J. Nishii, S. Ito, A patterned TiO_2 (anatase)/TiO_2 (rutile) bilayer type photocatalyst: effect of the anatase/rutile junction on the photocatalytic activity, Angew. Chem., 114 (2002) 2935–2937.

[7] S. Pal, A.M. Laera, A. Licciulli, M. Catalano, A. Taurino, Biphase TiO_2 microspheres with enhanced photocatalytic activity, Ind. Eng. Chem. Res., 53 (2014) 7931–7938.

[8] J. Yang, J. Zhang, L. Zhu, S. Chen, Y. Zhang, Y. Tang, Y. Zhu, Y. Li, Synthesis of nano titania particles embedded in mesoporous SBA-15: characterization and photocatalytic activity, J. Hazard. Mater., 137 (2006) 952–958.

[9] X.Z. Li, F.B. Li, Study of Au/Au^{3+}-TiO_2 photocatalysts toward visible photooxidation for water and wastewater treatment, Environ. Sci. Technol., 35 (2001) 2381–2387.

[10] K. Hofstadler, R. Bauer, S. Novalic, G. Heisler, New reactor design for photocatalytic wastewater treatment with TiO_2 immobilized on fused-silica glass fibers: photomineralization of 4-chlorophenol, Environ. Sci. Technol., 28 (1994) 670–674.

[11] X.Z. Li, H. Liu, L.F. Cheng, H.J. Tong, Photocatalytic oxidation using a new catalyst TiO_2 microsphere for water and wastewater treatment, Environ. Sci. Technol., 37 (2003) 3989–3994.

[12] F. Maillard, S. Schreier, M. Hanzlik, E.R. Savinova, S. Weinkauf, U. Stimming, Influence of particle agglomeration on the catalytic activity of carbon-supported Pt nanoparticles in CO monolayer oxidation, Phys. Chem. Chem. Phys., 7 (2005) 385–393.

[13] D. Chen, F. Huang, Y.B. Cheng, R.A. Caruso, Mesoporous anatase TiO_2 beads with high surface areas and controllable pore sizes: a superior candidate for high performance dye sensitized solar cells, Adv. Mater., 21 (2009) 2206–2210.

[14] D.M. Antonelli, J.Y. Ying, Synthesis of hexagonally packed mesoporous TiO_2 by a modified sol–gel method, Angew. Chem. Int. Ed., 34 (1995) 2014–2017.

[15] J.-M. Wu, Photodegradation of rhodamine B in water assisted by titania nanorod thin films subjected to various thermal treatments, Environ. Sci. Technol., 41 (2007) 1723–1728.

[16] I.A.W. Tan, A. La Ahmad, B.H. Hameed, Adsorption of basic dye on high-surface-area activated carbon prepared from coconut husk: equilibrium, kinetic and thermodynamic studies, J. Hazard. Mater., 154 (2008) 337–346.

[17] C. Reitz, J. Reinacher, P. Hartmann, T. Brezesinski, Polymer-templated ordered large-pore mesoporous anatase–rutile TiO_2: Ta nanocomposite films: microstructure, electrical conductivity, and photocatalytic and photoelectrochemical properties, Catal. Today, 225 (2014) 55–63.

[18] D. Grosso, G.J.A.A. De Soler-Illia, F. Babonneau, C. Sanchez, P.A. Albouy, A. Brunet-Bruneau, A.R. Balkenende, Highly organized mesoporous titania thin films showing mono-oriented 2D hexagonal channels, Adv. Mater., 13 (2001) 1085–1090.

[19] E. Beyers, P. Cool, E.F. Vansant, Stabilisation of mesoporous TiO_2 by different bases influencing the photocatalytic activity, Microporous Mesoporous Mater., 99 (2007) 112–117.

[20] B. Mazinani, A. Beitollahi, A.K. Masrom, N. Yahya, T.S.Y. Choong, S.M. Ibrahim, J. Javadpour, Characterization and evaluation of the photocatalytic properties of wormhole-like

mesoporous silica incorporating TiO_2, prepared using different hydrothermal and calcination temperatures, Res. Chem. Intermed., 38 (2012) 1733–1742.
[21] B. Mazinani, A.K. Masrom, A. Beitollahi, R. Luque, Photocatalytic activity, surface area and phase modification of mesoporous SiO_2–TiO_2 prepared by a one-step hydrothermal procedure, Ceram. Int., 40 (2014) 11525–11532.
[22] T. Maschmeyer, F. Rey, G. Sankar, J.M. Thomas, Heterogeneous catalysts obtained by grafting metallocene complexes onto mesoporous silica, Nature, 378 (1995) 159–162.
[23] I.N. Germanovich, N.N. Dorozhkin, I.M. Kabel'skii, Ultrasonic impregnation of porous sintered components, Powder Metall. Met. Ceram., 1 (1964) 375–378.
[24] C. Li, Y. Wang, Y. Guo, X. Liu, Y. Guo, Z. Zhang, Y. Wang, G. Lu, Synthesis of highly ordered, extremely hydrothermal stable SBA-15/Al-SBA-15 under the assistance of sodium chloride, Chem. Mater., 19 (2007) 173–178.
[25] D. Zhao, J. Feng, Q. Huo, N. Melosh, G.H. Fredrickson, B.F. Chmelka, G.D. Stucky, Triblock copolymer syntheses of mesoporous silica with periodic 50 to 300 angstrom pores, Science, 279 (1998) 548–552.
[26] P. Van Der Voort, M. Benjelloun, E.F. Vansant, Rationalization of the synthesis of SBA-16: controlling the micro-and mesoporosity, J. Phys. Chem. B., 106 (2002) 9027–9032.
[27] M. Thommes, K. Kaneko, A.V. Neimark, J.P. Olivier, F. Rodriguez-Reinoso, J. Rouquerol, K.S.W. Sing, Physisorption of gases, with special reference to the evaluation of surface area and pore size distribution (IUPAC Technical Report), Pure Appl. Chem., 87 (2015) 1051–1069.
[28] A.V. Manole, M. Dobromir, R. Apetrei, V. Nica, D. Luca, Surface characterization of sputtered N: TiO_2 thin films within a wide range of dopant concentration, Ceram. Int., 40 (2014) 9989–9995.
[29] Y. Wang, J. Zhang, X. Liu, S. Gao, B. Huang, Y. Dai, Y. Xu, Synthesis and characterization of activated carbon-coated SiO_2/TiO_2-*x*C*x* nanoporous composites with high adsorption capability and visible light photocatalytic activity, Mater. Chem. Phys., 135 (2012) 579–586.
[30] Z.L. Hua, J.L. Shi, L.X. Zhang, M.L. Ruan, J.N. Yan, Formation of nanosized TiO_2 in mesoporous silica thin films, Adv. Mater., 14 (2002) 830–833.
[31] D.R. Sahu, L.Y. Hong, S.-C. Wang, J.-L. Huang, Synthesis, analysis and characterization of ordered mesoporous TiO_2/SBA-15 matrix: effect of calcination temperature, Microporous Mesoporous Mater., 117 (2009) 640–649.
[32] X. Gao, I.E. Wachs, Titania–silica as catalysts: molecular structural characteristics and physico-chemical properties, Catal. Today, 51 (1999) 233–254.
[33] M. Kruk, M. Jaroniec, A. Sayari, New insights into pore-size expansion of mesoporous silicates using long-chain amines, Microporous Mesoporous Mater., 35 (2000) 545–553.
[34] A.R. Oki, Q. Xu, B. Shpeizer, A. Clearfield, X. Qiu, S. Kirumakki, S. Tichy, Synthesis, characterization and activity in cyclohexene epoxidation of mesoporous TiO_2–SiO_2 mixed oxides, Catal. Commun., 8 (2007) 950–956.
[35] Z. Li, B. Hou, Y. Xu, D. Wu, Y. Sun, W. Hu, F. Deng, Comparative study of sol-gel-hydrothermal and sol–gel synthesis of titania–silica composite nanoparticles, J. Solid State Chem., 178 (2005) 1395–1405.
[36] B. Mazinani, A. Beitollahi, A.K. Masrom, S. Ibrahim, F. Jamil, The Effect of Aging Temperature on the Pores of Mesoporous SBA-15 Silica, AIP Conf. Proc., 2012, doi:10.1063/1.4769150.
[37] M. Addamo, V. Augugliaro, A. Di Paola, E. García-López, V. Loddo, G. Marcì, R. Molinari, L. Palmisano, M. Schiavello, Preparation, characterization, and photoactivity of polycrystalline nanostructured TiO_2 catalysts, J. Phys. Chem. B., 108 (2004) 3303–3310.
[38] M. Wu, G. Lin, D. Chen, G. Wang, D. He, S. Feng, R. Xu, Sol-hydrothermal synthesis and hydrothermally structural evolution of nanocrystal titanium dioxide, Chem. Mater., 14 (2002) 1974–1980.
[39] C.-C. Wang, J.Y. Ying, Sol-gel synthesis and hydrothermal processing of anatase and rutile titania nanocrystals, Chem. Mater., 11 (1999) 3113–3120.
[40] M.A. Fox, M.T. Dulay, Heterogeneous photocatalysis, Chem. Rev., 93 (1993) 341–357.
[41] O.M. Alfano, M.I. Cabrera, A.E. Cassano, Photocatalytic reactions involving hydroxyl radical attack, J. Catal., 172 (1997) 370–379.
[42] G. Nagaraju, K. Manjunath, T.N. Ravishankar, B.S. Ravikumar, H. Nagabhushan, G. Ebeling, J. Dupont, Ionic liquid-assisted hydrothermal synthesis of TiO_2 nanoparticles and its application in photocatalysis, J. Mater. Sci., 48 (2013) 8420–8426.
[43] R. Zuo, G. Du, W. Zhang, L. Liu, Y. Liu, L. Mei, Z. Li, Photocatalytic degradation of methylene blue using TiO_2 impregnated diatomite, Adv. Mater. Sci. Eng., 2014 (2014).
[44] H.E. Byrne, W.L. Kostedt, J.M. Stokke, D.W. Mazyck, Characterization of HF-catalyzed silica gels doped with Degussa P25 titanium dioxide, J. Non. Cryst. Solids, 355 (2009) 525–530.